Temperature-dependent structural and magnetic properties of (*x*) NiFe$_2$O$_4$+(1 − *x*)BaTiO$_3$ (0≤ *x* ≤ 1; **Δ** *x* = 0.1) multiferroic solid solutions

Prakash Bongurala[1] · Balaganesh Dharavath[1] · Venkataiah Gorige[1]

Abstract

Multi-functional materials such as two-phase particulate magnetoelectrics (MEs) are of recent interest due to their assuring device applications at ultra-low power consumption above room temperature. In the present work, high-quality solid solutions of NiFe$_2$O$_4$ (NFO) and BaTiO$_3$ (BTO) with different volume ratios were prepared by using the solid-state reaction route, and the conjunctive response of their physical properties was explored by studying structural and magnetic properties as a function of temperature. The temperature-dependent x-ray diffraction and Raman data clearly assure the effectiveness of the BTO lattice strain on the NFO phase. The agreement between the magnetic moment values estimated from structural, spectroscopic and magnetic data establishes the structure-property correlations in (*x*)NFO+(1 − *x*)BTO (*x* = 0 − 1; Δ *x* = 0.1) solid solutions. The change in magnetic parameters due to strain generated in BTO of these composites gives the scope for futuristic magnetic switching devices without applying any external magnetic field.

Keywords NiFe$_2$O$_4$ · BaTiO$_3$ · Magnetoelectrics · Multiferroics · Raman spectroscopy

1 Introduction

The magnetoelectric (ME) multiferroic materials are of immense interest due to their promising room-temperature (RT) low-power consumption applications in various suitable technologies [1–3]. These materials simultaneously possess magnetic and electric orders and show ME coupling, which enables us to control the magnetic response by applied electric field and electric response by applied magnetic field [3–6]. However, these fascinating ME based effects in a single phase materials are very rare and have been discovered only in few systems with incompatible transitions at adverse conditions [7, 8]. Alternatively, ME composites demonstrate relatively high ME coupling originating from strain, charge and orbital mediation across the interface of ferromagnetic (FM) and ferroelectric (FE) phases. Surprisingly, the individual phases of FMs and FEs do not exhibit ME property. In fact the strain mediated ME coupling emerges as a result of two phases as per the principle of product properties [9, 10]. Although, the most interesting object is to investigate the magnetic response of these ME composites by an application of electric field to realize them for possible RT device applications [11–13]. The key aspect of these ME materials is to prepare them without any third phase formation with a well-matched interface in any form such as heterostructured thin films, bi-layered laminates, particulate nano/bulk composites, etc. [13–25].

Among all the ferrites and FEs, the combination of Nickel ferrite, NiFe$_2$O$_4$(NFO) and Barium titanate, BaTiO$_3$(BTO) is the best suitable material system due to their intimate interface contact and promising ME coupling at RT [24–27]. Also, the BTO exhibits structural phase transitions from *cubic* (C) to *tetragonal* (T) to *orthorhombic* (O) to *rhombohedral* (R), at 393 K, 278 K and 193 K respectively, as the temperature is lowered [28, 29]. It gives an opportunity to study the temperature-dependent structural and physical properties to understand the nature of the underlying strain-induced effects in FE material, in general. The FM counterpart NFO, is known to be soft ferrite with low electrical conductivity and having magnetic transition temperature well above RT. At RT, the perovskite BTO exhibits T-phase with lattice parameters $a = 3.9938$ Å and $c = 4.0330$ Å; the NFO has a spinel structure having lattice parameter $a = 8.3357$ Å [26]. The NFO lattice parameter is almost twice that of pseudo cubic lattice parameter (4.0134 Å) of BTO,

---

✉ Venkataiah Gorige
    vgsp@uohyd.ac.in

1   School of Physics, University of Hyderabad, Gachibowli,
    Hyderabad 500046, Telangana, India

enabling the well-matched (mismatch $\approx$ 3.7%) interface formation with BTO at unit cell level.

The present paper demonstrates the correlation between structural, spectroscopic and magnetic parameters by investigating the temperature dependent x-ray diffraction (XRD), Raman and magnetization properties of $(x)NiFe_2O_4 + (1 − x)BaTiO_3$ ($0 \le x \le 1$ with $\Delta x = 0.1$) particulate composites. The details of these studies are presented in the following sections.

2 Experimental methods

The solid solutions of $(x)NiFe_2O_4 + (1 − x)BaTiO_3$ ($0 \le x \le 1$ with $\Delta x = 0.1$) were prepared by using conventional solid-state reaction method [26]. The phase formation of the synthesized samples were confirmed by performing the RT XRD measurements in the 2θ range, 10−90° by making use of (PANalytical XPert^3) powder diffractometer. The temperature-dependent XRD patterns were obtained at different temperatures viz., 570 K, 300 K, 230 K and 150 K corresponding to C, T, O and R phases of BTO, respectively. The temperature-dependent Raman measurements were performed using scanning near field optical microscope (SNOM) attached with micro-Raman microscope. The Nd:YaG laser with 532 nm wavelength was used as a source (in the back scatter geometry) in confocal Raman spectrometer. The scattered light was captured using CCD detector (model α-300 of WiTec, Germany) using an objective lens with 100X. The Raman measurements were performed on single phase and composite samples, and data were obtained at temperatures corresponding to distinct FE phases of BTO i.e., T at 300 K, O at 230 K and R at 150 K. The temperature-dependent magnetic responses were measured by using (Lakeshore) vibrating sample magnetometer in the temperature range, 300−700 °C at an applied external field of 250 Oe. The magnetic field dependent magnetic responses were obtained in the applied field range of 0− ±12 kOe at RT.

3 Results and discussion

3.1 X-ray diffraction

Figure 1(a) shows the XRD patterns of single-phase BTO ($x = 0$) sample measured at four different structural phases, i.e., R (150 K), O (230 K), T (300 K) and C (570 K). The obtained XRD data were compared with the corresponding ICDD files, 98-031-0174 for R, 98-006-6482 for O, 98-007-3646 for T and 98-009-5437 for C phases, respectively. The measured XRD patterns are found to match well with ICDD data files. It is clear from the XRD patterns that there is

no secondary peaks observed in the patterns, except for the pattern measured at 150 K (R-phase). The identified extra peaks are indicated with '∗' symbol in Fig. 1 and originates from the crystalline ice (H_2O), which is physisorbed on the samples during the measurement [30]. In fact, similar results were also found in the literature and it mainly arises due to insufficient vacuum in the measurement chamber. It is worth to observe from the XRD patterns (Fig. 1(b)) measured at 230 K and 300 K that certain peaks appear as doublets. These doublet splittings taking place in O and T phases of BTO is mainly due to different domain (viz., *a*-domain and *c*-domain) orientations [29].

Figure 1(c) shows the XRD data of NFO ($x = 1$) sample collected at 150 K, 230 K, 300 K and 570 K. It is clear from the figure that there are no secondary peaks, except those corresponding to NFO peaks. However, the data measured at 150 K show the crystalline ice (marked with '∗' symbol) related diffraction peaks, as discussed earlier in the case of $x = 0$ sample. It is clear from the figure that unlike $x = 0$ sample, the NFO ($x = 1$) sample does not show any change in the patterns of XRD measured at different temperatures. As, the NFO crystallizes in cubic structure, all the patterns measured at different temperatures were compared with standard ICDD data (file number 98-024-6894). It gives an impression that the NFO is not undergoing any structural change up to 570 K.

In a similar manner as that for BTO and NFO single phase samples, the XRD data of other composite samples ($x = 0.2, 0.4, 0.6$ and 0.8) were collected at 150 K, 230 K, 300 K and 570 K. Even for composites, no unwanted phase related diffraction peaks were detected. Now, to gain further knowledge on structural as well as lattice-strain related information, the XRD data were subjected to Rietveld's refinement by *HighScore Plus* software. The refinement was done for all the samples by assuming $R\bar{3}m$ (R), $Pm\bar{3}m$ (O), $P4mm$ (T), $Pmm2$ (C) space groups for the data obtained at temperatures 150 K, 230 K, 300 K, and 570 K, respectively. In the case of NFO, $Fd\bar{3}m$ space group was used for all the temperatures of investigation. These space groups were used for individual as well as composite samples. The goodness of fit (GOF), i.e., χ^2 parameter, which dictates the chosen simulated model agrees with the measured experimental data; in fact the χ^2 parameter values are found to be in agreeable range of acceptance. The Rietveld refined XRD patterns, typically for $x = 0.6$ sample is presented in Fig. 2. The obtained crystallographic parameters pertaining to the four different structural phases of BTO are congruent with literature [31, 32]. The refined crystallographic parameters are given in Table 1. It is worth to notice from the table that the lattice parameters of BTO and NFO individual ($x = 0$ and 1) samples were found to be smaller compared to phases present

Table 1 The refined crystallographic parameters of $(x)NiFe_2O_4 + (1 − x)BaTiO_3$ ($0 \leq x \leq 1$) samples at different temperatures, corresponding to different structural phases of $BaTiO_3$

x	T (K)	BTO				NFO	GOF
		a (Å)	b (Å)	c (Å)	strain % ($\times 10^{-2}$)	a (Å)	χ^2
0	570	4.0101	4.0101	4.0101	–	–	1.2
	300	3.9945	3.9945	4.0334	06.53	–	1.4
	230	3.9869	4.0134	4.0191	09.03	–	2.8
	150	4.0036	4.0036	4.0036	16.00	–	4.5
0.2	570	4.0107	4.0107	4.0107	–	8.3459	1.5
	300	3.9985	3.9985	4.0264	07.21	8.3379	1.1
	230	3.9901	4.0086	4.0194	11.50	8.3340	2.3
	150	4.0049	4.0049	4.0049	14.50	8.3319	3.5
0.4	570	4.0111	4.0111	4.0111	–	8.3467	1.3
	300	3.9981	3.9981	4.0284	07.32	8.3389	1.1
	230	3.9903	4.0102	4.0201	10.60	8.3361	1.9
	150	4.0057	4.0057	4.0057	13.60	8.3337	3.7
0.6	570	4.0105	4.0105	4.0105	–	8.3449	1.2
	300	3.9978	3.9978	4.0275	06.59	8.3374	1.1
	230	3.9904	4.0100	4.0193	09.41	8.3348	1.6
	150	4.0047	4.0047	4.0047	14.00	8.3318	3.4
0.8	570	4.0108	4.0108	4.0108	–	8.3452	1.1
	300	3.9985	3.9985	4.0275	06.66	8.3378	1.2
	230	3.9909	4.0106	4.0192	09.85	8.3350	1.4
	150	4.0051	4.0051	4.0051	14.30	8.3321	2.0
1	570	-	-	-	–	8.3474	1.3
	300	-	-	-	–	8.3374	1.3
	230	-	-	-	–	8.3348	1.1
	150	-	-	-	–	8.3310	2.7

in composites. Also, *a*, *b* and *c* parameters were increasing with an increase of temperature for BTO and NFO materials in composites. The present observation may be ascribed to the increased tensile stress of BTO unit cell and its effect on NFO unit cell [33–35]. However, as the present composite is composed of polycrystalline NFO and BTO phases, it becomes difficult to see the net strain effect, generated in BTO, on NFO phase, due to random orientation of these lattice cells.

It is worth mentioning from Table 1 that while cooling the sample from 570 K to lower temperatures, the BTO exhibits structural transformation at 393 K thereby changing from C-phase ($a = b = c; \alpha = \beta = \gamma = 90°$) to T-phase by expanding in *c*−direction and contracting in *a*, *b*−directions, resulting in $a = b \neq c$. Upon further decreasing the temperature, the sample changes its T-phase to O-phase thereby changing the lattice parameters as given, $a \neq b \neq c$. Further decreasing the temperature of the sample, it changes from O to R-phase with $a = b = c$ and $\alpha = \beta = \gamma \neq 90°$. It gives a clear impression that the BTO induces distinct strain states pertaining to the different structural phases. Therefore,

to investigate the effect of lattice-strain that originates from BTO due to different structural phases on the NFO phase, the volume strain of the BTO has been estimated by using unit cell volumes. The below mentioned formula has been used to estimate the percentage of volume-strain,

$$Strain\% = \frac{\Delta V}{V_C} = \frac{V_C - V_P}{V_C} \times 100 \tag{1}$$

where, V_C is the volume of BTO in C-phase, V_P is the volume in different FE (T-, O-, R-) phases of BTO. The estimated strain percentages are given in Table 1 and are found to increase with the decrease of temperature, i.e., the strain in BTO increases as it changes from C-phase to T-phase to O-phase to R-phase, continuously. The consequence of these strain-states were clearly visible as jumps in temperature-dependent magnetization measurements of these composites, reported earlier [26]. Further, it was anticipated that the generated lattice-strain in BTO has significant impact on physical properties of NFO, particularly on the magnetization. Also, the magnetization of spinel ferrites is highly

susceptible to changes in cation arrangement between tetrahedral (*Th*) and octahedral (*Oh*) sites of NFO. Therefore, an effort has been made to estimate the cation arrangement of NFO from the selected XRD reflection intensities. In the present case, (220), (400), and (440) planes were taken into consideration to estimate cation distribution in NFO [36]. The intensity ratios of these planes were estimated theoretically and corroborated with experimentally obtained intensity ratios as per the relation given below,

$$\frac{I_{hkl}^{exp}}{I_{h'k'l'}^{exp}} = \frac{I_{hkl}^{cal}}{I_{h'k'l'}^{cal}} \tag{2}$$

here, I_{hkl}^{exp} and I_{hkl}^{cal} are the experimental and theoretical intensities of (*hkl*) plane, respectively. The theoretical intensities were computed using the following process [36–38].

$$I_{hkl}^{cal} = |F_{hkl}|^2 N L_p \tag{3}$$

where, $|F_{hkl}|$, N and L_p are the structure factor, multiplicity factor and Lorentz polarization factor, respectively. The L_p was defined as

$$L_p = \frac{1 + cos^2 2\theta_{hkl}}{sin^2\theta_{hkl} cos\theta_{hkl}} \tag{4}$$

The θ_{hkl} is Bragg diffraction angle relating to a particular (*hkl*) plane. The structure factor is defined as

$$F_{hkl} = \sum f.e^{-M} \tag{5}$$

Now, e^{-M} is the Debye-Waller factor and f is scattering factor, given as

$$\sum f = \sum_{i=1}^{3} a_i e^{\frac{-b_i sin^2\theta_{hkl}}{\lambda^2}} + c \tag{6}$$

where, a, b and c are the constants taken from the international crystallographic tables [39]. The parameter λ, is corresponding to wavelength of x-rays. In the above equation, M is determined as

$$M = \frac{6h^2 T}{mk_B\theta_D^2}\left[\psi(x) + \frac{x}{4}\right]\frac{sin^2\theta}{\lambda^2} \tag{7}$$

Here, h is the Planck's constant, T is absolute temperature at which measurement is carried out, k_B is Boltzmann constant, θ_D is Debye temperature, and $x = \frac{\theta_D}{T}$. The parameter m, is given as $m = \frac{A}{N_A}$, where A is atomic weight and N_A is the Avogadro's number, respectively. The factor $[\psi(x) + \frac{x}{4}]$ in equation 7 was estimated based on the protocol laid by James [37]. The Debye temperature values, 378 K and 357 K have been considered for A and B sites, respectively [40].

The cation arrangement (*y*) of NFO in composite samples was calculated by making use of the measured XRD data at different temperatures [36, 37, 40]. Surprisingly, it has been noticed that the estimated value of *y* is found to be zero thereby indicating no Ni^{2+} ion present in the *Th* site. That means the Ni ions are found to show their presence only in the *Oh* site. Hence, $[Ni_yFe_{1-y}]_{Th}[Ni_{1-y}Fe_{1+y}]_{Oh}O_4 \Rightarrow [Ni_0Fe_{1-0}]_{Th}[Ni_{1-0}Fe_{1+0}]_{Oh}O_4(\because y = 0) \Rightarrow [Fe]_{Th}[NiFe]_{Oh}O_4$. It is clear from this analysis that in an inverse spinel structure, the Fe^{3+} $(3d^5)$ ions with magnetic moment $5\mu_B$ are in the *Th* site with ferromagnetically ordered (first) sublattice. Whereas the Fe^{3+} $(3d^5)$ and Ni^{2+} $(3d^8)$ ions with magnetic moment $5\mu_B$ and $2\mu_B$, respectively, are in the *Oh* site with ferromagnetically ordered second sublattice. Now, these two sublattices are antiferromagnetically coupled by resulting in the net magnetic moment of $2\mu_B$ per formula unit. That means the net magnetic moment is arising from Ni^{2+} ions of *Oh* site of the unit cell and is in unison with the earlier reports [32, 36].

The magnetic moment values estimated from XRD are found to match well with the values estimated from magnetic data (discussed in the next section). As it was mentioned earlier, although, significant amount of strain is developed in BTO unit cell due to structural phase transition of BTO, no effect is seen on cation distribution (estimated as bulk property) of NFO thereby no change in magnetic moment as a function of BTO content in the composite. It may be also true that the effect of strain generated in BTO is not sufficient enough to observe the substantial changes in the cation distribution of NFO; however, it is anticipated that the effect is quite visible in Raman measurements.

3.2 Raman spectroscopy

Raman spectroscopy is an excellent technique to estimate the associated vibrational modes of the atoms present in differently distinct sites in a unit cell. In the present case, Raman data is useful to estimate the cation distribution in the NFO at temperatures representing to distinct FE/structural phases of BTO. As the Raman measurements are sensitive than the XRD measurements, and thus particular analysis gives a scope to complement the results obtained from XRD data. Also, the effect of lattice-strain originated from BTO on NFO could be studied. Therefore, the Raman spectroscopy measurements of all the samples were performed at different temperatures, (viz., 300 K, 230 K and 150 K) corresponding to the three distinct FE (T, O and R) phases of BTO, respectively. The Raman spectra of BTO and NFO samples measured at 300 K, 230 K and 150 K are shown in Fig. 3(a and c).

In general, the single phase BTO exhibits the fifteen atomic vibrations. Out of these fifteen vibrations, seven are infrared (IR) active ("$3A_1 + 4E$") and eight are Raman active ("$3A_1 + B_1 + 4E$"). Again, the Raman active modes are of two kinds, which are longitudinal optical (LO) and transverse optical (TO). However, it is difficult to differentiate the LO and TO modes of vibrations [41, 42]. Here (see Fig. 3(b)), the $A_1(TO)$, B_1 modes represent atomic vibrations along $z-$direction and E modes depict the atomic vibrations along $x-$, $y-$directions. The $A_1(TO1)$ mode infers the Raman mode originating while six Oxygen (O) atoms and one Titanium (Ti) atom are vibrating with respect to Barium (Ba) atom. The $A_1(TO2)$ mode represents the Raman mode developing when O1 atoms and Ti atom are vibrating with respect to O2 atoms. The $A_1(TO3)$ mode originates while six O atoms and Ti atom are vibrating with respect to Ba atoms. The B_1 mode refers to the Raman shift when O2 atoms are vibrating against each other, in the direction perpendicular to the plane of these O2 atoms. The $E(TO1)$ mode refers to the Raman shift arising when six O atoms, Ti atom are vibrating in $y-$direction with respect to Ba atoms. The $E(TO2)$ mode refers to the Raman shift arising when six O atoms and Ti atoms are vibrating along $x-$direction with respect to Ba atoms. The $E(TO3)$ and $E(TO4)$ modes correspond to the two O2 atoms vibrating against O1 in y and x-directions, respectively. All these modes are schematically represented in Fig. 3(b).

Figure 3(a) shows the Raman spectra of single-phase BTO at 150 K, 230 K and 300 K. It is clear from the figure that the single-phase BTO displays seven Raman active modes, viz., "E(TO2), A_1(TO1), B_1, E(TO3), E(TO4), A_1(TO2) and A_1(TO3)", at 190, 252, 310, 350, 489, 530 and 718 cm^{-1} respectively. The E(TO1) mode is not present in plot as it's position is below the measurement limit. From the obtained Raman spectra, the full-width at half-maxima (FWHM) of the Raman modes were obtained. The spectral broadening (or FWHM) is observed to be increasing with increase of temperature for all the spectral peaks as the BTO undergoes structural change from R to T phase. This behavior is attributed to FWHM broadening, which is related to the lifetime of phonon. The FWHM is inversely proportional to the phonon life time [43]. The B_1 and A_1(TO2) modes are showing shift towards lower frequency side while structure of the BTO changes from R to T. This behavior is attributed to the increment of lattice parameter c (see Table 1), which will contribute to the tensile stress in z-direction of BTO unit cell. The A_1(TO1) mode is found to shift towards higher frequency side with increase in temperature and the noticed behavior is attributed to compressive stress among the corresponding atoms of BTO unit cell in z-direction.

In general, NFO exhibits ten atomic vibrational modes, in which five are infrared active ("$5T_{1u}$") and remaining five vibrations are Raman active ("$A_g + E_g + 3T_{2g}$") [44, 45]. Here (see Fig. 3(d)), the A_g mode infers to the symmetric extension of "O" atoms along $Fe - O$ in Th site. The E_g mode represents the symmetric bending of O and nickel (Ni) atoms in different directions. The $3T_{2g}$ modes refer to the O and Ni atoms vibrating in three different directions [45].

Figure 3(c) shows the Raman spectra of single-phase NFO at different temperatures. It demonstrates five Raman active modes, i.e., "$T_{2g}(1)$, E_g, $T_{2g}(2)$, $T_{2g}(3)$ and A_{1g}" at 204, 333, 487, 575 and 702 cm^{-1} respectively. A careful observation of $T_{2g}(2)$, E_g and A_{1g} modes clearly reveal the shoulder like behavior from the low frequency side of peaks. These shoulder modes arise from the Oh sites consisting of Ni^{2+} and Fe^{3+} ions [44]. The $T_{2g}(2)$, E_g and A_{1g} modes shift towards the lower wavenumber side with increase in temperature of NFO sample. This particular shift has been attributed to the elongation of the lattice parameter of NFO with increase in temperature [46].

Raman spectra of composites ($x = 0$ to 1) was measured at three structural phases of BTO, and patterns are presented in the Fig. 4. In the composites, A_1(TO2) and A_1(TO3) modes corresponding to BTO are showing the shift towards low-frequency side with the increment of NFO content in composites. When strain is released, then shift towards low frequency side will be observed in the particular mode [47], that means tensile stress is present in the BTO unit cell [46]. This tensile stress is evidenced from the XRD data (table 1), lattice parameters of BTO are increasing with increment of NFO content in composites. In the prepared samples, corresponding BTO modes are shifting towards lower frequency, indicating the strain released from NFO is affecting BTO and ultimately peak shift is observed for the modes corresponding to BTO. The A_1(TO1) mode is showing shift towards higher frequency side with increment of NFO content in composites. This behaviour may be due to the NFO grains getting compressed due to BTO. However, the modes corresponding to NFO are not showing any shift with increase in BTO content in composites.

The Raman spectral data has been used to estimate the cation distribution based on their vibrational modes. The Raman data of composite samples were fitted with Lorentz function and a representative plot in the case of $x = 0.8$ is presented in Fig. 5. The peaks associated with NFO and BTO Raman modes are shown in different color dotted curves, respectively. The magnetic moment per formula unit was estimated using the intensities of $A_{1g}(3)$ and $A_{1g}(2)$ modes.

Table 2 Magnetic moment (μ) per formula unit values calculated from Raman pattern of $(x)NiFe_2O_4 + (1-x)BaTiO_3$ $(0 \leq x \leq 1)$ composites

x	Temperature (K)	y	$\mu(\mu_B)$
0.8	300	0.0230	2.14
0.8	230	0.0289	2.17
0.8	150	0.0313	2.19
0.9	300	0.0221	2.13
0.9	230	0.0200	2.12
0.9	150	0.0184	2.11
1	300	0.0154	2.09
1	230	0.0364	2.22
1	150	0.0594	2.36

$$y = \frac{I(A_{1g}(3))}{I(A_{1g}(3)) + I(A_{1g}(2))} \tag{8}$$

Here, y is a cation distribution for mixed spinel structure.

$$[Ni_yFe_{1-y}]_T[Ni_{1-y}Fe_{1+y}]_OO_4 \tag{9}$$

The Raman modes of NFO are visible prominently only for x = 0.8, 0.9 and 1 samples. The magnetic moment per formula unit was estimated for these samples and are tabulated in Table 2 and room-temperature values are shown in Fig.7(b). These values are found to match well with the magnetic moments estimated from magnetization data.

3.3 Magnetization

In the prospective of understanding the effect of BTO on the magnetic response of NFO, the temperature-dependent magnetic $(M-T)$ measurements for all the samples $(0 \leq x \leq 1)$ have been undertaken in the applied field of 250 Oe. The measured $M-T$ curves in the temperature range, $300-700$ °C is shown in Fig. 6(a). In general, the thermal agitation will disturb the orientation of the magnetic moments along a given axis to zero at Curie
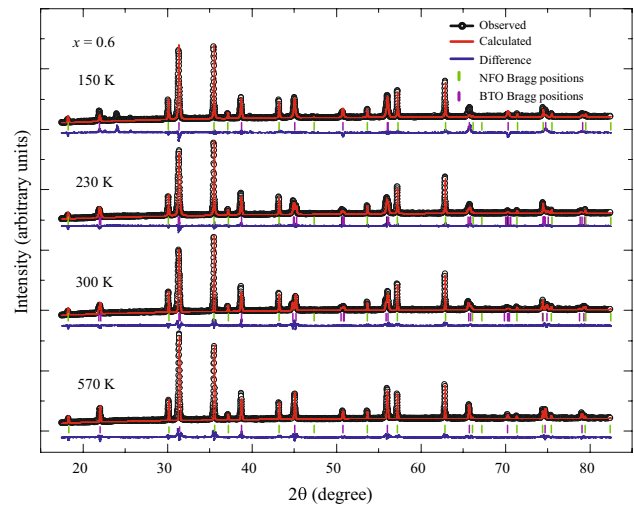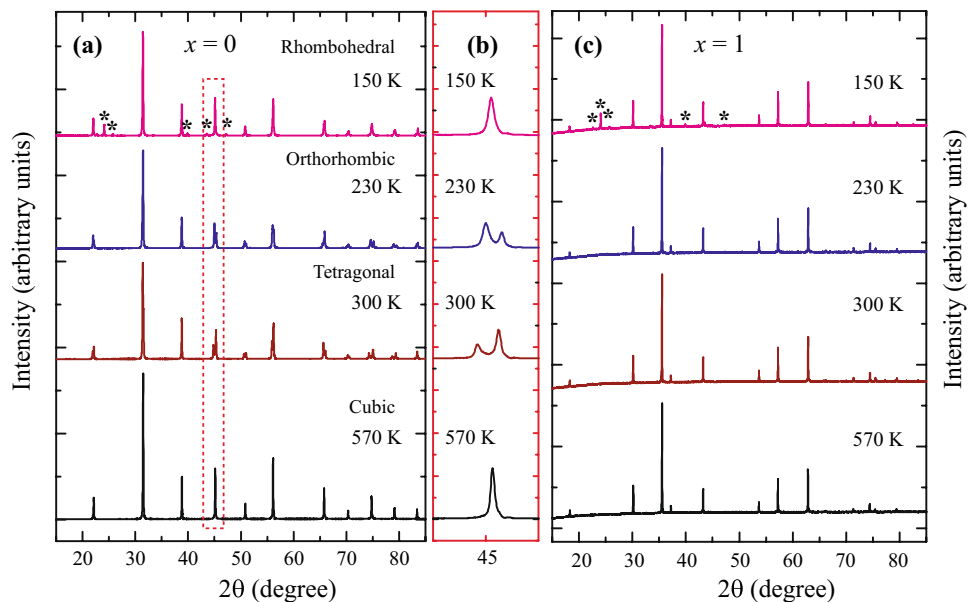

Fig. 2 Rietveld refined patterns of $x = 0.6$ composite sample at different temperatures

Fig. 1 The XRD patterns of (**a**) BTO ($x = 0$) (**b**) enlarged view at $2\theta \approx 45°$ and (**c**) NFO ($x = 1$) samples at 150 K, 230 K, 300 K and 570 K, respectively
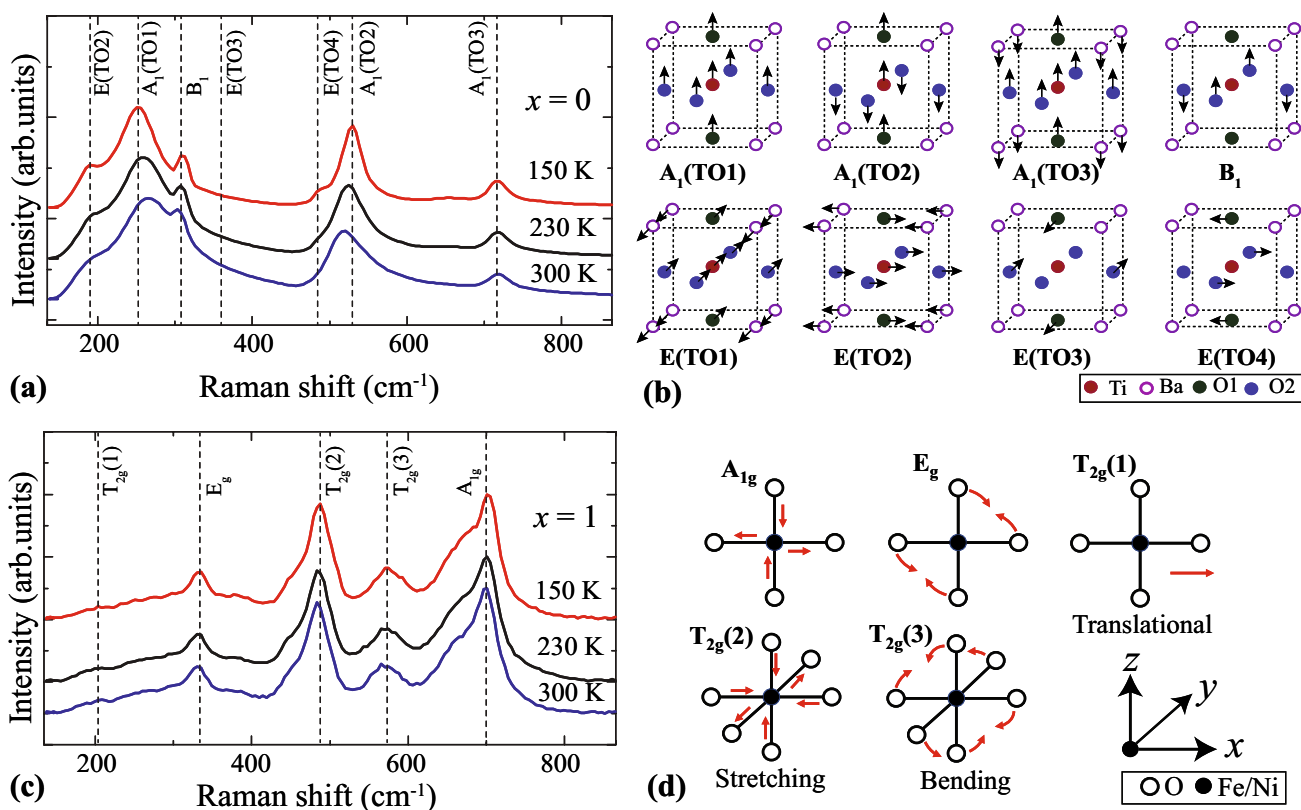
Fig. 3 (a and c) The Raman vibrational patterns at different temperatures and (b and d) schematic representations of possible vibrational modes of BTO and NFO samples

temperature (T_C). The T_C values for all the composite ($0.1 \leq x \leq 1$) samples were obtained from the minima of dM/dT versus T data of respective $M - T$ curves. The variation of T_C with NFO content (x) has been shown in Fig. 6(b). At first, it is clear from the figure that the observed T_C values are found to be in agreement with the earlier reports of (x)NFO+$(1 - x)$BTO composites [32, 48]. In the present investigation, the T_C values are increasing with the increase of NFO content (x) and the observed behavior is ascribed to the reduced diffusion of non magnetic phase into the NFO phase matrix. The reduced non magnetic phase percolation may enhance the (super)exchange interaction in NFO phase. The enhanced exchange interaction may lead to a strong ferrimagnetic state, which is less affected by thermal field, resulting in enhanced T_C with increasing NFO content (x). It is interesting to note from the figure that a small hump was noticed at about 420 °C for all composite samples, including $x = 1$ (NFO) sample. The hump becomes significant as the NFO content is increasing in the composites. In fact, similar observations were also made by

other researchers and they attributed it to the enhanced exchange interaction in the samples [48, 49]. In the present case, it may likely be magnetic anisotropy dominating over the exchange interaction as the temperature decreases below 420 °C. The magnetic domains will rest in their preferred orientations (magnetic anisotropy) by dominating the exchange interaction. The effect decreases with increasing BTO content in the composites. However, these observations require much more analysis and experimental evidence to support our arguments.

Figure 7(a) shows that magnetic response ($M - H$) curves of composite samples ($0.1 \leq x \leq 1$) measured at 300 K, where BTO is in FE (T) phase. With a view to corroborate the magnetic moment values obtained from previous (XRD and Raman measurements) sections, the magnetic moment per formula unit were calculated for all the samples and their variation with x is shown in Fig. 7(b). The obtained magnetic moment values well matches with the values obtained from XRD and Raman measurements. The agreement of these magnetic moment values with the theoretically estimated ones ($2\mu_B/f.u.$)
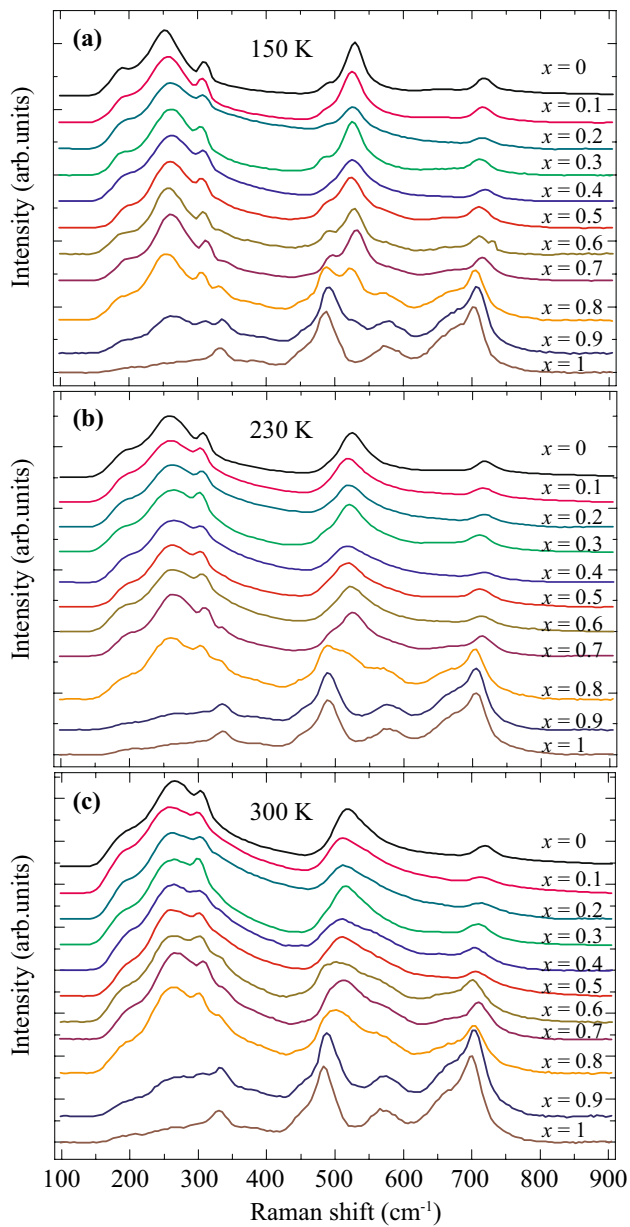
Fig. 4 Raman patterns of composites $(x = 0 \text{ to } 1)$ at temperatures (**a**) 150 K, (**b**) 230 K and (**c**) 300 K
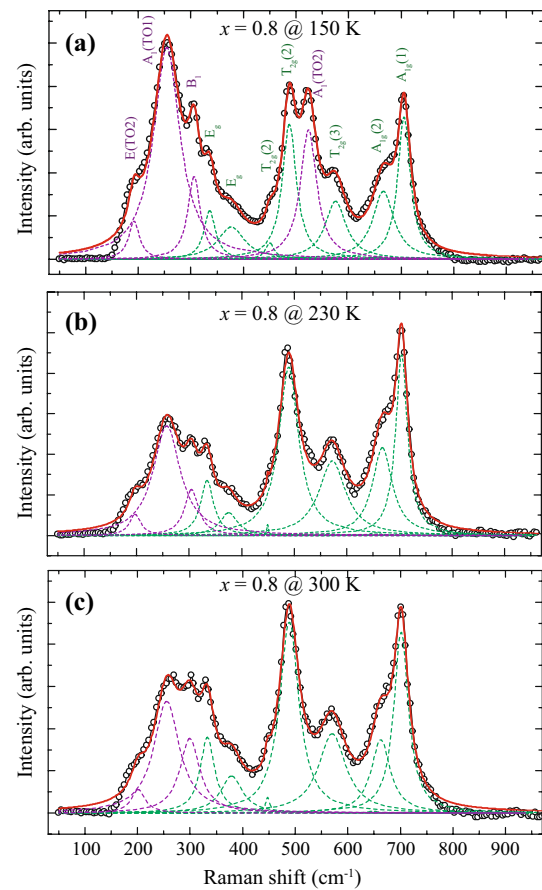

Fig. 5 Raman patterns of 0.8NFO+0.2BTO composite sample at temperatures 150 K, 230 K and 300 K (the deconvoluted modes are shown as dotted line)

confirms cubic inverse spinel structure of NFO in the composites. This result also infers the strong structure-property correlations in composites. Although, due to soft magnetic nature, the exchange interactions are dominant in NFO sample, the NFO in composites may have significant magnetic anisotropy. In fact, the mentioned anisotropy arises due to the BTO content. Therefore, to understand the effect of BTO on magnetic response of NFO in composites, the corresponding effective magnetic

anisotropy constant (k_e) values were evaluated by fitting the experimental data (initial $M - H$ curve) to the following law of approach to saturation equation, which is given below [36],

$$M = M_S\left(1 - \frac{a}{H^2}\right) + \chi_p H \tag{10}$$

here, M, M_S, H and χ_p are the magnetization, saturation magnetization, applied magnetic field and paramagnetic susceptibility respectively. The parameter a is given by

$$a = \frac{8}{150}\frac{k_e^2}{\mu_0^2 M_S^2} \tag{11}$$

here, k_e and μ_0 are the effective anisotropy constant and free space permeability respectively. The variation of estimated effective anisotropy constant values as a function of NFO content is shown in Fig. 7(c) and the values are in good
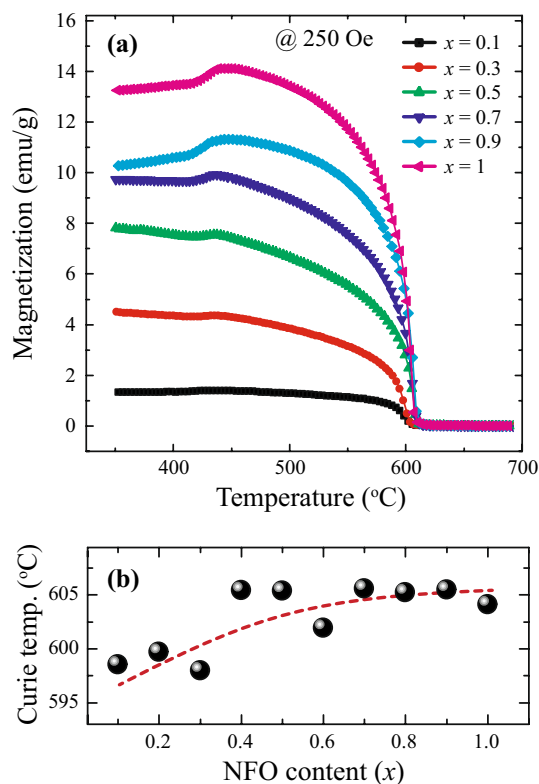
Fig. 6 (**a**) Temperature-dependent magnetization $(M-T)$ curves and (**b**) variation of T_C with NFO content (x) in (x)NFO+$(1-x)$BTO composites

congruence with the earlier reports in the case of NFO [36]. The k_e values are found to increase with the increase of NFO content and it is attributed to the reduction of non-magnetic phase content in the matrix of NFO ferrimagnetic phase.

4 Conclusion

The temperature-dependent XRD data clearly reveals that the different structural phases of BTO have different strain-states, the effect of this strain on NFO structural parameters is found to be minimal. The magnetic moment per formula unit values estimated from x-ray diffraction, Raman spectroscopy and magnetization measurements are in consistence with each other and in good agreement with the theoretically estimated values and hence it establishes the structure-property correlations in (x)NFO + $(1-x)$BTO ($x = 0-1$; $\Delta x = 0.1$) composites. The change in magnetic parameters due to strain generated in BTO in these composites enable us to realise the room-temperature magnetoelectric based devices.
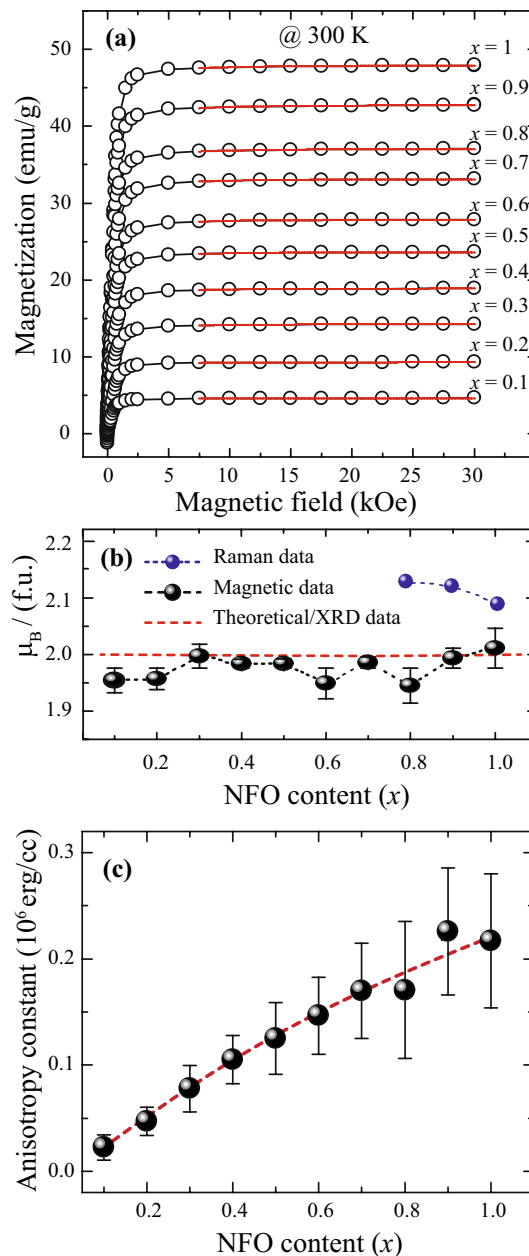

Fig. 7 (**a**) Room-temperature $M-H$ curves and the red solid line shows the law of approach to saturation curve fit, (**b**) variation of magnetic moment (μ_B) per formula unit with NFO content (x) and (**c**) variation of cubic anisotropy constant with NFO content (x) in (x)NFO+$(1-x)$BTO composites

Declarations

Conflict of interest: All authors of this manuscript declare that no conflict of interests exists.

References

1. J. Ma, J.M. Hu, Z. Li, C.W. Nan, Recent progress in multiferroic magnetoelectric composites: from bulk to thin films. Adv Mater **23**, 1062 (2011). https://doi.org/10.1002/adma.201003636

2. M.N.U. Haq, V.V. Shvartsman, V. Samulionis, M. Ivanov, J. Banys, D.C. Lupascu, Dependence of the magnetoelectric coupling on elastic and dielectric properties of two-phase multiferroic composites. J Mater Sci **56**, 14978 (2021). https://doi.org/10.1007/s10853-021-06271-9

3. D.K. Pradhan, S. Kumari, P.D. Rack, Magnetoelectric composites: applications, coupling mechanisms and future directions. Nanomaterials **10**, 2072 (2020). https://doi.org/10.3390/nano10102072

4. W. Eereinstein, N.D. Mathur, J.F. Scott, Multiferroic and magnetoelectric materials. Nature **442**, 759 (2006). https://doi.org/10.1038/nature05023

5. V. Laguta, M. Kempa, V. Bovtun, J. Bursik, K. Zhai, Y. Sun, S. Kamba, Magnetoelectric coupling in multiferroic Z-type hexaferrite revealed by electric field modulated magnetic resonance studies. J Mater Sci **55**, 7624 (2020). https://doi.org/10.1007/s10853-020-04563-0

6. X. Mu, H. Zhang, C. Zhang, S. Yang, J. Xu, Y. Huang, J. Xu, Y. Zhang, Q. Li, X. Wang, D. Cao, S. Li, Poly(vinylidene fluoride-trifluoroethylene)/cobalt ferrite composite films with a self-biased magnetoelectric effect for flexible AC magnetic sensors. J Mater Sci **56**, 9728 (2021). https://doi.org/10.1007/s10853-021-05937-8

7. N.A. Hill, Why are there so few magnetic ferroelectrics? J Phys Chem B **104**, 6694 (2000). https://doi.org/10.1021/jp000114x

8. M. Fiebig, Revival of the magnetoelectric effect. J Phys D: Appl Phys **38**, R123 (2005). https://doi.org/10.1088/0022-3727/38/8/R01

9. J.V. Suchtelen, Product properties: A new application of composite materials. Philips Res Rep **27**, 28 (1972). https://ci.nii.ac.jp/naid/10016561394/en/

10. C.W. Nan, M.I. Bichurin, S. Dong, D. Viehland, G. Srinivasan, Multiferroic magnetoelectric composites: Historical perspective, status, and future directions. J Appl Phys **103**, 031101 (2008). https://doi.org/10.1063/1.2836410

11. X. Liang, C. Dong, H. Chen, J. Wang, Y. Wei, M. Zaeimbashi, Y. He, A. Matyushov, C. Sun, N. Sun, A review of thin-Film magnetoelastic materials for magnetoelectric applications. Sensors **20**, 1532 (2020). https://doi.org/10.3390/s20051532

12. M.J. Bauer, A. Thomas, B. Isenberg, J. Varela, A. Faria, D.P. Arnold, J.S. Andrew, Ultra-low-power current sensor utilizing magnetoelectric nanowires. IEEE Sens J **20**, 5139 (2020). https://ieeexplore.ieee.org/document/8963976

13. T. Taniyama, Electric-field control of magnetism via strain transfer across ferromagnetic/ferroelectric interfaces. J Phys: Condens Matter **27**, 504001 (2015). https://doi.org/10.1088/0953-8984/27/50/504001

14. N. Adhlakha, K.L. Yadav, R. Singh, $BiFeO_3$-$CoFe_2O_4$-$PbTiO_3$ composites: structural, multiferroic and optical characteristics. J Mater Sci **50**, 2073 (2015). https://doi.org/10.1007/s10853-014-8769-z

15. L. Hao, D. Zhou, Q. Fu, Y. Hu, Multiferroic properties of multilayered $BaTiO_3$-$CoFe_2O_4$ composites via tape casting method. J Mater Sci **48**, 178 (2013). https://doi.org/10.1007/s10853-012-6726-2

16. J.X. Zhang, J.Y. Dai, W. Lu, H.L.M. Chan, Room temperature magnetic exchange coupling in multiferroic $BaTiO_3$/$CoFe_2O_4$ magnetoelectric superlattice. J Mater Sci **44**, 5143 (2009). https://doi.org/10.1007/s10853-009-3512-x

17. P. Zhou, Z. Zheng, Y. Qi, G. Srinivasan, T. Zhang, Magnetoelectric effect in $Ni_{1-x}Zn_xFe_2O_4$/PZT thin film heterostructures. Phys Lett A **426**, 127897 (2022). https://doi.org/10.1016/j.physleta.2021.127897

18. Z. Zheng, P. Zhou, Y. Liu, K. Liang, R.G. Tanguturi, H. Chen, G. Srinivasan, Y. Qi, T. Zhang, Strain effect on magnetoelectric coupling of epitaxial NFO/PZT Heterostructure. J Alloys Compd **818**, 152871 (2020). https://doi.org/10.1016/j.jallcom.2019.152871

19. M. Breitenbach, K. Dorr, S.G. Ebbinghaus, Magnetoelectric properties of $Co_{1-x}Ni_xFe_2O_4$/$BaTiO_3$ heterostructures with 3–3 connectivity obtained by eutectic crystallization. Phys Status Solidi B **257**, 1900618 (2020). https://doi.org/10.1002/pssb.201900618

20. A.B. Swain, K.S. Dinesh, V. Subramanian, P. Murugavel, Engineering resonance modes for enhanced magnetoelectric coupling in bilayer laminate composites for energy harvesting applications. Phys Rev Appl **13**, 024026 (2020). https://doi.org/10.1103/PhysRevApplied.13.024026

21. F.L. Zabotto, F.P. Milton, A.J. Gualdi, A.J.A. de Oliveira, J.A. Eiras, D. Garcia, Magnetodielectric and magnetoelectric correlation in (1–x)PMN-PT/xCFO 0–3 particulate composites. J Alloys Compd **829**, 154517 (2020). https://doi.org/10.1016/j.jallcom.2020.154517

22. M.D. Rather, R. Samad, N. Hassan, B. Want, Magnetodielectric effect in rare earth doped $BaTiO_3$-$CoFe_2O_4$ multiferroic composites. J Alloys Compd **794**, 402 (2019). https://doi.org/10.1016/j.jallcom.2019.04.244

23. Z. Zhai, Z.P. Xing, S.X. Dong, J.F. Li, D. Viehland, Magnetoelectric Laminate Composites: An Overview. J Am Ceram Soc **91**, 351 (2008). https://doi.org/10.1111/j.1551-2916.2008.02259.x

24. K.S. Dinesh, S. Gupta, A.B. Swain, V. Subramanian, M.K. Padmanabhan, R.L. Mahajan, Large converse magnetoelectric effect in Sm doped $Pb(Mg_{1/3}Nb_{2/3})$-$PbTiO_3$ and $NiFe_2O_4$ laminate composite. J Alloys Compd **858**, 157684 (2021). https://doi.org/10.1016/j.jallcom.2020.157684

25. V. Gorige, R. Kati, D.H. Yoon, P.S. Anil Kumar, Strain mediated magnetoelectric coupling in a $NiFe_2O_4$-$BaTiO_3$ multiferroic composite. J Phys D: Appl Phys **49**, 405001 (2016). https://doi.org/10.1088/0022-3727/49/40/405001

26. P. Bongurala, V. Gorige, Structural magnetic and electric properties of multiferroic $NiFe_2O_4$-$BaTiO_3$ composites. J Magn Magn Mater **477**, 350 (2019). https://doi.org/10.1016/j.jmmm.2018.12.014

27. P. Bongurala, Das A. Mrinalini, V. Gorige, Dielectric and electron spin resonance studies of $(x)NiFe_2O_4 + (1 − x)BaTiO_3$ ($0 \le x \le 1$) magnetoelectric composites. J Alloys Compd **903**, 163931 (2022). https://doi.org/10.1016/j.jallcom.2022.163931

28. G. Venkataiah, Y. Shirahata, M. Itoh, T. Taniyama, Manipulation of magnetic coercivity of Fe film in Fe/$BaTiO_3$ heterostructure by electric field. Appl Phys Lett **99**, 102506 (2011). https://doi.org/10.1063/1.3628464

29. G. Venkataiah, E. Wada, T. Taniguchi, M. Itoh, T. Taniyama, Electric-voltage control of magnetism in Fe/BaTiO$_3$ heterostructured multiferroics. J Appl Phys **113**, 17C701 (2013). https://doi.org/10.1063/1.4793511

30. J.J. Shephard, S. Ling, G.C. Sosso, A. Michaelides, B. Slater, C.D. Salzmann, Is high-density amorphous ice simply a "derailed" state along the ice I to ice IV pathway? J Phys Chem Lett **8**, 1645 (2017). https://doi.org/10.1021/acs.jpclett.7b00492

31. M.K. Lee, T.K. Nath, C.B. Eom, M.C. Smoak, F. Tsui, Strain modification of epitaxial perovskite oxide thin films using structural transitions of ferroelectric BaTiO$_3$ substrate. Appl Phys Lett **77**, 3547 (2000). https://doi.org/10.1063/1.1328762

32. B. Sarkar, B. Dalal, V.D. Ashok, K. Chakrabarthi, A. Mitra, S.K. De, Magnetic properties of mixed spinel BaTiO$_3$- NiFe$_2$O$_4$ composites. J Appl Phys **115**, 123908 (2014). https://doi.org/10.1063/1.4869782

33. R.N. Bhowmik, G. Vijayasri, R. Ranganathan, Structural characterization and ferromagnetic properties in Ga^{3+}doped α-Fe$_2$O$_3$ system prepared by coprecipitation route and vacuum annealing. J Appl Phys **116**, 123905 (2014). https://doi.org/10.1063/1.4896482

34. C. Jacinto, T. Catunda, D. Jaque, J.G. Sole, A.A. Kaminiskii, Thermal lens spectroscopy through phase transition in neodymium doped strontium barium niobate laser crystals. J Appl Phys **101**, 023113 (2007). https://doi.org/10.1063/1.2430938

35. C. Peng, Y. Zhang, Z.W. Cheng, X. Cheng, J. Meng, Nitrate$^-$citrate combustion synthesis and properties of Ce$_{1-x}$Sm$_x$O$_{2-0.5x}$ solid solutions. J Mater Sci Mater Electron **13**, 757 (2002). https://doi.org/10.1023/A:1021556431397

36. K.K. Bestha, J.J. Abraham, J.A. Chelvane, V. Gorige, Influence of cation distribution on magnetic response of polycrystalline Co$_{1-x}$Ni$_x$Fe$_2$O$_4$ (0$\leq$ x $\leq$1) ferrites. Phys Scr **95**, 085802 (2020). https://doi.org/10.1088/1402-4896/aba3d2

37. R.W. James, The optical principles of the diffraction of x-rays, (G. Bell & Sons, London, 1962)

38. K.B. Modi, T.K. Pathak, N.H. Vasoya, V.K. Lakhani, G.J. Baldha, P.K. Jha, X-ray Debye temperature of mechanically milled Ni$_{0.5}$Zn$_{0.5}$Fe$_2$O$_4$ spinel ferrite. Indian J Phys **85**,411 (2011). https://doi.org/10.1007/s12648-011-0051-5

39. E. Prince, International tables for crystallography, Vol. C (Wiley, New York, 2004), p 578

40. C.S. Kim, S.W. Lee, S.I. Park, J.Y. Park, Y.J. Oh, Atomic migration in Ni-Co ferrite. J Appl Phys **79**, 5428 (1996). https://doi.org/10.1063/1.362328

41. A. Wei, L.T. Hui, W.C. Hai, D.C. Ling, L.N. Neng, L. Yong, Q.Z. Ming, S. Tao, W.Y. Yin, J. Huan, T.G. Shan, J.X. Ping, Assignment for vibrational spectra of BaTiO$_3$ ferroelectric ceramic based on the first-principles calculation. Acta Phys Chim Sin **31**, 1059 (2015). https://doi.org/10.3866/PKU.WHXB201504144

42. Y. Li, S.D. Zhou, L. Zhu, H. Wu, Y.G. Wang, F.M. Pan, Optimization of multiferroic properties in BiFeO$_3$-BaTiO$_3$-based ceramics by tuning oxygen octahedral distortion. J Mater Sci **55**, 2750 (2020). https://doi.org/10.1007/s10853-019-04244-7

43. N. Khatun, Rajput P. Anita, D. Bhattacharya, S.N. Jha, S. Biring, S. Sen, Anatase to rutile phase transition promoted by vanadium substitution in TiO$_2$: A structural, vibrational and optoelectronic study. Ceram Int **43**, 14128 (2017). https://doi.org/10.1016/j.ceramint.2017.07.153

44. Z.Z. Lazarevic, C. Jovalekic, D. Sekulic, M. Slankamenac, M. Romcevic, A. Milutinovic, N.Z. Romcevic, Characterization of nanostructured spinel NiFe$_2$O$_4$ obtained by soft mechanochemical Synthesis. Sci of Sinter **44**, 331 (2012). https://doi.org/10.2298/SOS1203331L

45. M.N. Iliev, D. Mazumdar, J.X. Ma, A. Gupta, F. Rigato, J. Fontcuberta, Monitoring B-site ordering and strain relaxation in NiFe2O4 epitaxial films by polarized Raman spectroscopy. Phys Rev B **83**, 014108 (2011). https://doi.org/10.1103/PhysRevB.83.014108

46. F. Urena, S.H. Olsen, L. Siller, U. Bhaskar, T. Pardoen, J.P. Raskin, Strain in silicon nanowire beams. J Appl Phys **112**, 114506 (2012). https://doi.org/10.1063/1.4765025

47. R. Djemour, A. Redinger, M. Mousel, L. Gutay, X. Fontane, V.I. Roca, A.P. Rodriguez, S. Siebentritt, The three A symmetry Raman modes of kesterite in Cu$_2$ZnSnSe$_4$. Opt Express **21**, A695 (2013). https://doi.org/10.1364/OE.21.00A695

48. J.P. Zhou, L. Lv, Q. Liu, Y.X. Zhang, P. Liu, Hydrothermal synthesis and properties of NiFe$_2$O$_4$@BaTiO$_3$ composites with well-matched interface. Sci Technol Adv Mater **13**, 045001 (2012). https://doi.org/10.1088/1468-6996/13/4/045001

49. K.K. Patankar, S.S. Joshi, B.K. Chougule, Dielectric behaviour in magnetoelectric composites. Phys Lett A **346**, 337 (2005). https://doi.org/10.1016/j.physleta.2005.06.099

Publisher's Note Springer Nature remains neutral with regard to jurisdictional claims in published maps and institutional affiliations.